SCIENTIFIC REPORTS

Relationship between High-frequency Radiation and Asperity Ruptures, Revealed by Hybrid Back-projection with a Non-planar Fault Model

Ryo Okuwaki[1], Yuji Yagi[2] & Shiro Hirano[3]

[1]Graduate School of Life and Environmental Sciences, University of Tsukuba, 1-1-1 Tennodai, Tsukuba, Ibaraki 305-8572, Japan, [2]Faculty of Life and Environmental Sciences, University of Tsukuba, 1-1-1 Tennodai, Tsukuba, Ibaraki 305-8572, Japan, [3]Faculty of Engineering, Information and Systems, University of Tsukuba, 1-1-1 Tennodai, Tsukuba, Ibaraki 305-8573, Japan.

High-frequency seismic waves are generated by abrupt changes of rupture velocity and slip-rate during an earthquake. Therefore, analysis of high-frequency waves is crucial to understanding the dynamic rupture process. Here, we developed a hybrid back-projection method that considers variations in focal mechanisms by introducing a non-planar fault model that reflects the subducting slab geometry. We applied it to teleseismic P-waveforms of the Mw 8.8 2010 Chile earthquake to estimate the spatiotemporal distribution of high-frequency (0.5–2.0 Hz) radiation. By comparing the result with the coseismic slip distribution obtained by waveform inversion, we found that strong high-frequency radiation can precede and may trigger a large asperity rupture. Moreover, in between the large slip events, high-frequency radiation of intermediate strength was concentrated along the rupture front. This distribution suggests that by bridging the two large slips, this intermediate-strength high-frequency radiation might play a key role in the interaction of the large slip events.

High-frequency radiation during rupture on a fault is a phenomenon that is crucial to understanding the dynamic rupture process of an earthquake. High-frequency radiation can be generated by an abrupt change of rupture velocity[1,2]. Pioneering studies[3,4] numerically calculated high-frequency (> 1 Hz) radiation by using ray theory and showed that discontinuities of slip-rate and rupture velocity contribute equally to high-frequency radiation.

Waveform inversions have been applied to many earthquakes to reveal the spatiotemporal distribution of coseismic slip[5–8]. High-frequency components, however, are difficult to reproduce by conventional waveform inversions due to uncertainties of Green's function. Yagi and Fukahata[7] developed an inversion formulation by introducing the uncertainty of Green's function. By solving an inverse problem with the new formulation that considers data covariance components of waveforms due to the modeling error of Green's function, high-frequency components of observed waveforms are well reproduced in the synthetic waveforms. However, fine discretization of the assumed fault model, for which numerous computational resources are required to solve the inverse problem, is necessary to represent small-scale heterogeneities that can radiate high-frequency waves. Specifically, if grid intervals are made N times finer, then the computational resources required to solve the inverse problem are $O(N^6)$ times larger. Thus, waveform inversion using high-frequency waveforms of a great earthquake based on a fault model with fine discretization may be unrealistic for now.

The back-projection (BP) method[9] is a tool to estimate the spatiotemporal distribution of high-frequency radiation by simply stacking high-frequency components of observed waveforms with the predicted travel-time shifts. The BP method is based on the assumption that seismograms have coherence among stations of a regional array[10] and this assumption is satisfied for high-frequency waves below about 2 Hz[11] for the spacing and apertures of the current regional arrays. By using the BP method, the spatiotemporal distribution of high-frequency radiation can be inferred without calculating Green's functions. Because this feature reduces the computational power needed, fine discretization can easily be achieved with the BP method. To date, the BP method has been applied in investigations of many great earthquakes (e.g., the 2004 Sumatra-Andaman[9], the 2008 Wenchuan[12], the 2010 Chile[13], and the 2011 Tohoku[14] earthquakes). However, it is not possible to understand the whole rupture

process of an earthquake by use of the BP method alone, because interpretation of what the images obtained by the BP method represent physically is ambiguous[15], and because resolution of the BP method may become worse, especially for shallow earthquakes, owing to the effects of reflected phases[16] (e.g., pP and sP phases). The BP method is useful for inferring the sources of high-frequency radiation and roughly visualizing rupture propagation under the condition that the peak amplitude of stacked waveforms is obtained at the direct P-phase[15] (e.g., for a deep-focus earthquake[17]). If the peak amplitude is obtained at the reflected phases, instead of the P-phase, the BP image smears out or distributes at inappropriate timing and space[15]. Though some pioneering studies[18,19] have analyzed the source process using both the BP method and waveform inversion, integration of the BP method with waveform inversion may lead to misinterpretation owing to the spatiotemporal uncertainty of the BP images.

The hybrid back-projection (HBP) method[16] is an improvement of the BP method. The HBP method stacks the cross-correlation functions of the observed waveforms with the corresponding theoretical Green's functions to estimate the spatiotemporal distribution of high-frequency sources. The cross-correlating process should mitigate the effect of reflected phases and detect the direct P-phase, thus making it possible to constrain the depth of the seismic source area. Green's functions, however, depend on the depth and focal mechanism (strike, dip, and rake angle) of the source point. Thus, to obtain a high-resolution image with the HBP method, it is essential to employ a fault model with accurate geometry.

In this study, we further developed the HBP method by introducing a non-planar fault model that approximates the geometry of a subducting plate interface[20]. We then applied the modified HBP method to teleseismic P-waveforms of the moment magnitude M_w 8.8 earthquake that occurred off the Maule region, south-central Chile, on 27 February 2010 and estimated the spatiotemporal distribution of the sources of high-frequency radiation. We then compared the sources of high-frequency radiation with the coseismic slip distribution obtained previously for that earthquake[21]. Because the HBP method makes it possible to visualize a less biased image of the spatiotemporal distribution of high-frequency sources at high resolution, precise integration of the high-frequency sources with the coseismic slip distribution is possible. Finally, we discussed a relationship between high-frequency radiation and large-asperity ruptures.

Results

Data. The observed waveforms used in this study were downloaded from the Data Management Center of the Incorporated Research Institute for Seismology (IRIS). We selected vertical component of teleseismic (epicentral distance between 30–100°) waveforms at 122 stations for a Main application (M_w 8.8, 2010 Chile earthquake, Fig. 1a), and those at 66 stations for a Test application (M_w 7.1, 2012 Chile earthquake, see Supplementary Fig. S1 online). We applied a high-frequency (0.5–2.0 Hz) band-pass filter to both the observed waveforms and the Green's functions. We adopted $N = 3.5$ for the Nth root stacking to the cross-correlation function of the observed waveforms and theoretical Green's functions for all observation stations. The data were shifted and aligned by the first arrivals of P-waves (Fig. 1b). The instrument response was deconvolved to velocity. We calculated the theoretical Green's functions for teleseismic body waves[22] with a sampling rate of 20 Hz. The travel times, the geometrical spreading factors and the ray parameters were calculated with the ak135 model[23]. We calculated Green's functions with a 1-D structural velocity model[24] for near source area, which was modified and used previously for inversion of the 2010 Chile earthquake[21] (see Supplementary Table S1 online). The non-planar fault model is extracted from the subducting-slab geometry of the SLAB model[20]. The way of construction of the non-planar fault model is described in detail in the Methods section.

Test application to the 2012 Chile (M_w 7.1) earthquake. Before applying the modified HBP method to the M_w 8.8 2010 Chile earthquake, we evaluated the resolution of the method by applying it to the M_w 7.1 earthquake occurred off the Maule, Chile, on 25 March 2012. This earthquake was the largest inter-plate aftershock following the 2010 Chile earthquake (M_w 8.8)[25]. The epicentre of this earthquake (72.217°W, 35.200°S, as determined by the local seismic station network of the Centro Sismológico Nacional (CSN), http://www.sismologia.cl; last access on 18 October, 2014) was 152 km northeast of the 2010 Chile earthquake epicentre. The non-planar fault model (Fig. 2a) is 303 km long and 303 km wide, and the source grid has 3 km spacing. Figure 2b shows snapshots at 4 s intervals of the spatial distribution of high-frequency radiation obtained by using the HBP method. The amplitude of the stacked signals on each source grid cell was normalized by the maximum amplitude among all grid cells in space and time. After the initiation of
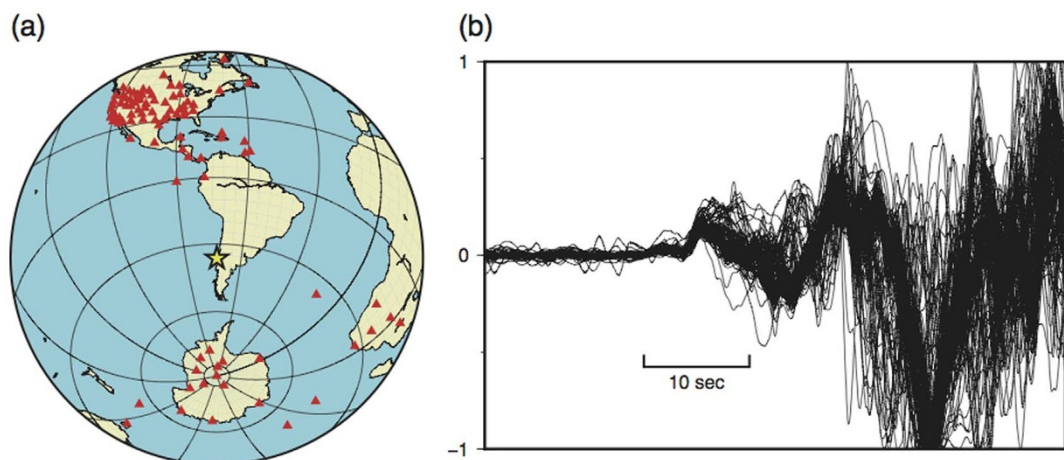

Figure 1 | Teleseismic station distribution and P-waveform traces of the M_w 8.8 2010 Chile earthquake. (a) Observation stations (triangles) for analysis of the HBP method, and the epicentre (star) of the 2010 Chile earthquake determined by CSN. (b) Traces of the unfiltered vertical component of P-waveforms of the 2010 Chile earthquake observed at 122 teleseismic stations (downloaded from IRIS, aligned by the first P-phase arrivals, and normalized by the maximum of the absolute amplitude of each waveform). The panel (a) was generated by using the Generic Mapping Tools[36].
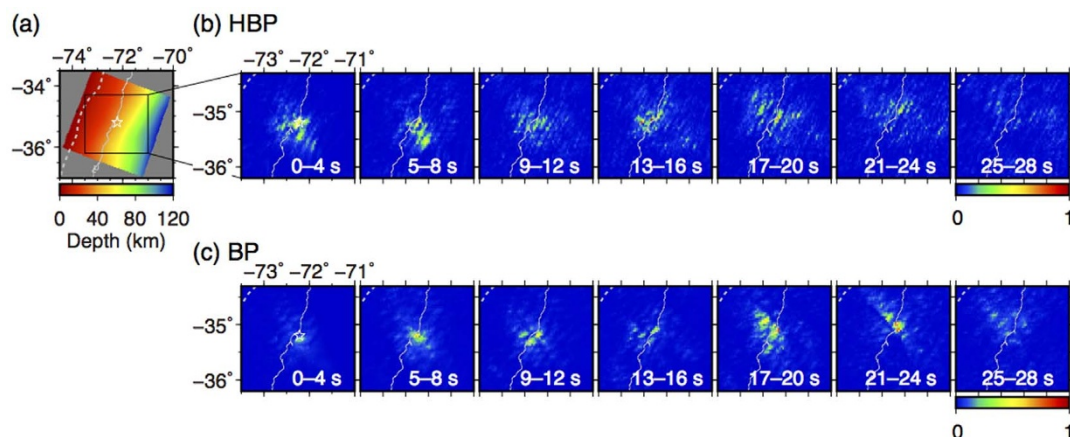
Figure 2 | Non-planar fault model and snapshots of the distribution of high-frequency radiation of the M_w 7.1 2012 Chile earthquake obtained by the HBP and BP methods. (a) The geometry of the non-planar fault model. Snapshots of spatiotemporal distribution of high-frequency radiation obtained by (b) the HBP method and (c) the BP method. The color scale represents normalized amplitudes, and warmer colors show relatively stronger high-frequency radiation. The star indicates the epicentre of the 2012 Chile earthquake determined by CSN. The dashed line and white lines are the trench location and the coastline, respectively.

rupture, high-frequency radiation was excited at the hypocentre, and diminished after about 24 s. The sources of high-frequency radiation are concentrated at the hypocentre occupying an area of about 50 km × 50 km. To confirm the resolution of the HBP method, we compared our result with one obtained by using the conventional BP method with a non-planar fault model. In the BP method (Fig. 2c), high-frequency radiation still lasted until 28 s after the hypocentral time and this duration is longer than the one of the HBP result. In the panels of 17–28 s (Fig 2c), sources of high-frequency radiation extend toward north-westward from the hypocentre in the BP result and this extension is not apparent in the HBP result. The discrepancies of images between the BP and HBP method are generated by an effect of the reflected phases in the BP method, as has been previously discussed in a study of a shallow thrust earthquake[16] and a numerical simulation[15]. Therefore, our method developed in this study provides a high-resolution image of high-frequency radiation.

Main application to the 2010 Chile (M_w 8.8) earthquake. We next applied our method to the waveforms of the M_w 8.8 2010 Maule, Chile, earthquake. The epicentre (73.239°W, 36.290°S) was estimated by CSN. The non-planar fault model for this earthquake is 495 km long and 255 km wide, and the source grid has 3 km spacing (Fig. 3a). Figure 3b shows snapshots at 15 s intervals of the spatial distribution of high-frequency sources. Initially (Fig. 3b, in

the panel of 0–15 s), relatively strong high-frequency radiation occurred near the hypocentre, occupying an area of about 50 km × 50 km. Then, from about 30 s, high-frequency radiation of weak strength started to propagate northward in the along-strike direction at a speed of about 3.5 km/s. At around 70 s (Fig. 3b, in the panel of 61–75 s), another strong high-frequency radiation was generated at 180 km north-northeast of the hypocentre. The source of the second strong high-frequency radiation was distributed in an area of about 70 km × 50 km. This second high-frequency radiation source was diminished soon after its occurrence. Then, relatively weak high-frequency radiation was distributed around 200 km north-northeast of the hypocentre and vanished at about 100 s after the hypocentral time. Thus, with the HBP method, we found two strong high-frequency radiation sources, one near the hypocentre, and the other 180 km north-northeast of the hypocentre, as well as small patches of sources of weak high-frequency radiation distributed in-between the two strong high-frequency radiation sources and after the second strong high-frequency radiation source.

For evaluating the dependence of the HBP results on the velocity model, we obtained HBP images using two other velocity models: a model with no sea layer and a semi-infinite medium (see Supplementary Fig. S2). The spatiotemporal distribution of the HBP results for the two velocity models is slightly different from the original distribution, however the main characteristics do not
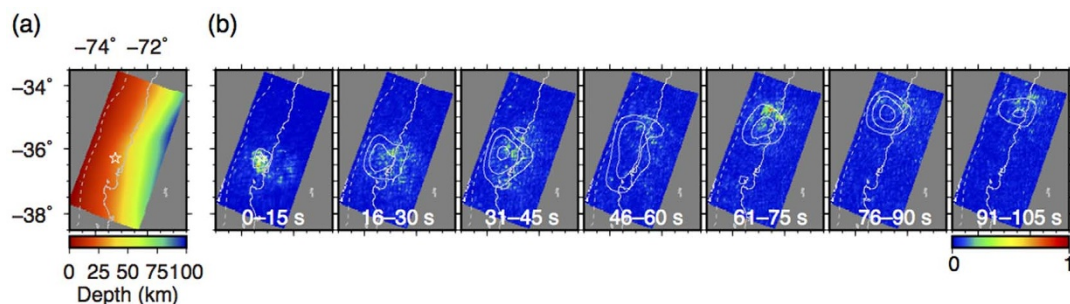

Figure 3 | Non-planar fault model and snapshots of the distribution of high-frequency radiation of the M_w 8.8 2010 Chile earthquake obtained by the HBP method. (a) The geometry of the non-planar fault model. (b) Snapshots of spatiotemporal distribution of high-frequency radiation obtained by the HBP method. The color scale represents normalized amplitudes, and warmer colors show relatively stronger high-frequency radiation. The star indicates the epicentre of the 2010 Chile earthquake determined by CSN. The dashed line and white lines are the trench location and the coastline, respectively. The distribution of average slip-rate within the corresponding time period is overlaid on the HBP result in (b) as white contours (contour intervals, 0.07 m/s).

change. This implies that the HBP image is mainly constrained by the radiation pattern and the predicted arrival time of dominant phases (P-, pP- and sP-phases). Next, we compared the HBP images using Green's functions calculated with different rake angles ($\pm 10°$ and $\pm 20°$ from the original rake angle in the main result, see Supplementary Fig. S3). We found that the results are robust against variations of the rake angle for this earthquake.

HBP and Inversion. We compared our HBP result for the 2010 Chile earthquake with the spatiotemporal distribution of coseismic slip obtained previously for the same earthquake by Pulido et al.[21], who estimated the spatiotemporal distribution of coseismic slip by using a waveform inversion taking into account the uncertainty of Green's function[7]. On the snapshots of the spatiotemporal distribution of high-frequency radiation (Fig. 3b), the coseismic slip is depicted as white contours. It can be seen that each strong high-frequency radiation event (the strong high-frequency radiation detected near the hypocentre at 0–15 s and about 180 km north-northeast of the hypocentre at 61–75 s) was followed by large slip occurring at right next to it (Fig. 3b). From about 30 to 60 s, in-between the first and second large slips, high-frequency radiation of weak strength was distributed along the northward rupture front obtained by the waveform inversion. Numerical study[4] shows that high-frequency waves can be generated by abrupt changes of rupture velocity and/or slip-rate, and our result likely reflects the nature of rupture propagation related to the high-frequency radiation.

HBP versus BP. There are some differences in the back-projected images of the 2010 Chile earthquake between those obtained by previous BP studies[11,13,26] and the HBP method in this study. With the BP method, relatively higher amplitudes of stacked high-frequency waves were obtained at about 20–30 s and at about 80–90 s after the hypocentral time[11,13]. By contrast, with the HBP method, relatively strong high-frequency radiation was obtained at near the initiation of rupture and at about 70 s after the hypocentral time (Fig. 3b). This discrepancy in the temporal distribution of strong high-frequency radiation can be explained by taking into account the systematic time delay in the BP method due to the large-amplitude reflected phases[15,16]. The time delay of the BP method is also observed in the result for the large 2012 Chile earthquake (M_w 7.1) as discussed in the Test application

subsection and predicted by previous studies[15,16]. To clarify the differences in the spatiotemporal distribution of high-frequency sources between the BP and the HBP images, we performed the BP analysis of the 2010 Chile earthquake and illustrated the distribution of high-frequency radiation obtained by using the BP and HBP methods as a function of distance from the hypocentre along strike direction and the time elapsed after the hypocentral time (Fig. 4). White contours of Figure 4 indicate the coseismic slip distribution obtained by previous study of waveform inversion[21]. For the BP analysis, the frequency band applied to the observed waveforms and assumed geometry of the non-planar fault model were the same as for the HBP analysis. The amplitude of the stacked signals on each source grid cell was normalized by the maximum amplitude among all grid cells in space and time. In both the BP and HBP results in Figure 4, the rupture mainly propagated northward from the hypocentre, which is consistent with the evolution of coseismic slip obtained by waveform inversion. In the HBP method (Fig. 4a), the relationship that the strong high-frequency radiation is followed by large slip is clearly seen. However in the BP method (Fig. 4b), the time delay in the BP method associated with the first (near the hypocentre, at 20–30 s) and second (about 200 km from the hypocentre, at 80–90 s) subevent is obvious. This time lag of the BP result compared to the HBP result is almost consistent with the time lag between the direct P-phase and sP-phase, and it may contribute to difficulty in understanding the relationship of the high-frequency radiation obtained by the BP method and the coseismic slip distribution obtained by waveform inversion. Diagonal streaks found in Figure 4b are known as a "swimming artifact" in the BP method, and this artifact can be mitigated by applying the reference window strategy[27].

Another difference between the BP and HBP results is found in the spatial distributions of high-frequency radiation sources. The sources of the high-frequency radiation in the previous BP studies[11,13,26] were obtained in the down-dip region from our result obtained by using the HBP method. In general, both the BP and HBP methods project the high-frequency sources relative to the epicentre. Because in this study we used the CSN epicentre located southwest of the U.S. Geological Survey (USGS) epicentre, our HBP result locates southwest from the previous BP results in which the USGS epicentre was used as the initial reference point. Our result obtained by using the HBP method is basically consistent with those
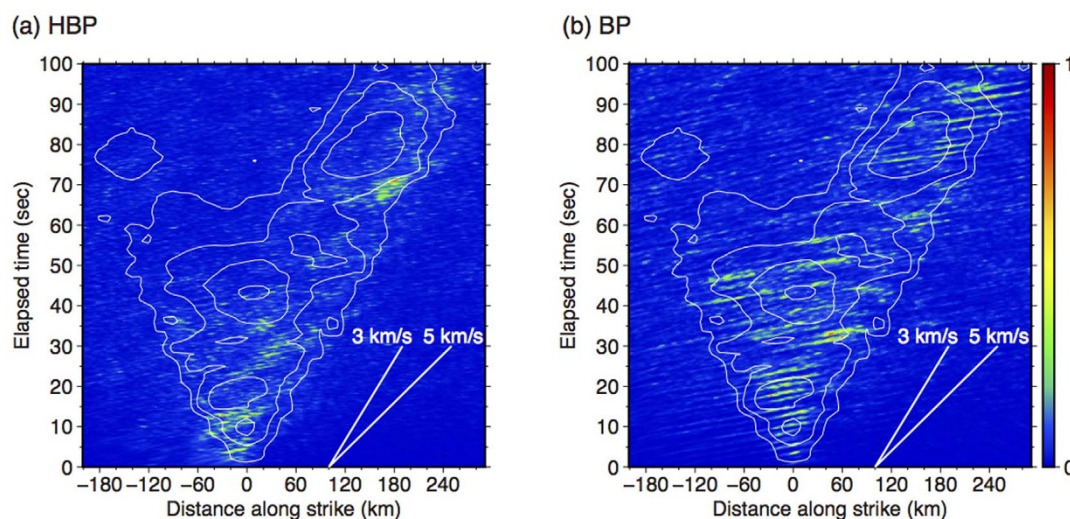

Figure 4 | Spatiotemporal evolution of high-frequency radiation and the coseismic slip of the 2010 Chile earthquake. Spatiotemporal evolution of high-frequency radiation of the 2010 Chile earthquake obtained by using (a) the HBP method and (b) the BP method. Hypocentral distance in the along-strike direction is shown on the abscissa, and elapsed time from the hypocentral time is shown on the ordinate. The color scale represents normalized amplitudes, and warmer colors show relatively stronger high-frequency radiation. The distribution of slip-rate is overlaid as white contours (contour intervals, 0.07 m/s). The epicentre (star) and rupture speeds (white lines) are also shown.

of other BP studies of the 2010 Chile earthquake if we take into account the effects due to large-amplitude reflected phases and the location of the initial break point, and the depth-dependent slip behavior reported by Lay et al.[18] is also recognized in this study.

The conventional BP has exploited the coherence of a regional array, while the HBP method is only applied to the global seismic data. In general, the resolution of the HBP and the BP images is improved as azimuthal coverage increases[15]. We performed the HBP and the BP analysis by using a regional array data to show the difference of the obtained images using the global network and the regional array data. As shown in Supplementary Figure S4, it is obvious that the resolution of both the HBP and the BP images is improved by using the global network compared to the regional array. This is because the relative travel-time shift between a grid point and the neighboring grid points can be more emphasized by using the global network rather than by using one regional array, and the resolution kernel of both the HBP and the BP images becomes tight.

Discussion

High frequency components can be radiated by both an abrupt change of rupture velocity and an abrupt change of slip-rate on a fault[4]. There is a relationship between rupture velocity and slip-rate[28,29], and the discontinuity of rupture velocity or slip-rate follows an abrupt change in space of fracture energy or stress drop[30,31]. Hence, the relationship between the high-frequency radiation and the large-asperity rupture found for the 2010 Chile earthquake suggests the discontinuity in fracture energy or stress distribution prior to the larger-asperity rupture. Although we cannot conclude which factor is dominant, a cascading asperity model[32] helps us understand the relationship between the strong high-frequency radiation and the large-asperity rupture if the discontinuity of fracture energy mainly contributes to it. In a cascading asperity model, the size of the asperity is proportional to the amount of fracture energy, and a large-asperity rupture is triggered by the rupture of a small asperity whose size is larger than the critical crack size of the large asperity as determined by the fracture energy[32]. On the basis of the cascading asperity model, the strong high-frequency radiation observed in this study is inferred to have been produced by the rupture of a relatively small asperity that may cascade up to the large-asperity rupture.

Another characteristic behavior of high-frequency radiation can be seen at 20–60 s after the hypocentral time (Fig. 4a). High-frequency radiation of weak strength is distributed in-between the first and second strong high-frequency events, near the hypocentre and at about 180 km north-northeast of the hypocentre, respectively. These weak high-frequency sources seem to be distributed along the edge of the northward-rupture front obtained by waveform inversion (Fig 4a). In a previous BP study of the 2010 Chile earthquake, Kiser and Ishii[13] reported that there was a gap in the high-frequency sources in-between the first and second subevents of high-frequency radiation, between 45 and 55 s after the hypocentral time. They argued that the rupture should propagate at high speed (7.5 km/s) in the gap, and they concluded that this gap was filled by the 2012 Chile earthquake[25] (M_w 7.1) occurred on 25 March 2012. In the HBP result, however, a relatively weak high-frequency source exists in this gap region (Fig. 4a); thus, we characterize this region as a bridge rather than as a gap. Numerical simulations have shown that fault roughness contributes to the perturbations of the rupture velocity that radiate high-frequency waves[33,34]. Therefore, a field that generates high-frequency radiation of weak strength may exist along the fault, causing the rupture velocity to fluctuate in-between the two large slips and possibly bridging them.

Methods

The HBP method. The HBP method[16], which is an improvement of the BP method, stacks the cross-correlation functions of the observed waveforms and the corresponding Green's functions for all observation stations. In the HBP method, we calculate the following quantities:

$$S_l^{\mathrm{HBP}}(t) = \left| s_l^{\mathrm{HBP}}(t) \right|^N \cdot \frac{s_l^{\mathrm{HBP}}(t)}{\left| s_l^{\mathrm{HBP}}(t) \right|}, \tag{1}$$

$$s_l^{\mathrm{HBP}}(t) = \sum_j A_j \left| w_{jl}(t) \right|^{\frac{1}{N}} \cdot \frac{w_{jl}(t)}{\left| w_{jl}(t) \right|}, \tag{2}$$

$$w_{jl}(t) = \frac{\dot{u}_j \,\hat{\times}\, \dot{G}_{jl}^{\mathrm{calc}}(t)}{\max\limits_{0 \le \alpha \le T} \sqrt{\int_0^T \dot{u}_j^2(\tau + \alpha) d\tau} \cdot \sqrt{\int_0^T (\dot{G}_{jl}^{\mathrm{calc}})^2(\tau) d\tau}}. \tag{3}$$

Equations (1) and (2) represent the Nth root stacking of the normalized cross-correlation function w_{jl} for all observation stations, where $\dot{u}_j$ is the observed waveforms at the jth station at time t, $\dot{G}_{jl}^{\mathrm{calc}}$ is the theoretical Green's function that is the deformation at the jth station generated by a unit impulse slip-rate at the lth source grid cell, $\hat{\times}$ denotes cross-correlation, s_l^{HBP} is a stacked trace of the Nth root of the cross correlation function, A_j is a normalizing parameter to prevent possible bias due to the distribution of the stations, and S_l^{HBP} is a Nth power of the s_l^{HBP}. We call the final form of the function of the HBP method, S_l^{HBP}, shown by equation (1) as the HBP value. A high-frequency Butterworth band-pass filter (0.5–2.0 Hz) is applied to the observed waveforms and the theoretical Green's functions before cross-correlating them. The observed waveform $\dot{u}$ is given by the summation of the convolution of the slip-rate $\dot{D}$ and the corresponding true Green's function $\dot{G}^{\mathrm{true}}$ for all source grid cells along the fault; thus, the cross-correlation function of equation (3) can be divided into two parts:

$$\dot{u}_j \,\hat{\times}\, \dot{G}_{jl}^{\mathrm{calc}}(t) = \sum_{l'} (\dot{D}_{l'} * \dot{G}_{jl'}^{\mathrm{true}}) \,\hat{\times}\, \dot{G}_{jl}^{\mathrm{calc}}(t)$$
$$= (\dot{D}_l * \dot{G}_{jl}^{\mathrm{true}}) \,\hat{\times}\, \dot{G}_{jl}^{\mathrm{calc}}(t) + \sum_{l' \neq l} (\dot{D}_{l'} * \dot{G}_{jl'}^{\mathrm{true}}) \,\hat{\times}\, \dot{G}_{jl}^{\mathrm{calc}}(t). \tag{4}$$

The first term on the right-hand side of equation (4) is the contribution from the potential lth grid cell, and the second term is the contribution from the other grid cells l' (except the lth grid cell). The contribution from the other grid cells is important for evaluating the resolution of the HBP method. We get high coherence of the cross-correlation function in the first term on the right-hand side of equation (4) if we calculate a better Green's function: one that is similar to the true Green's function. In the second term, the cross-correlation function of the true and the theoretical Green's functions has less coherence because we apply the high-frequency band-pass filter, which causes the difference between the true and theoretical Green's function to be emphasized. In general, non-linear Nth root stacking enhances the signal-to-noise ratio more than linear stacking[35]; thus, the contrast of coherence between the first and second term of equation (4) can be emphasized by the non-linear Nth root stacking. Therefore, we can detect the high-frequency sources at high resolution and the contribution of other grid cells, that is, the noise can be mitigated. If the cross-correlation function of the calculated Green's function $\dot{G}_{jl}^{\mathrm{calc}}$ and the true Green's function $\dot{G}_{jl}^{\mathrm{true}}$ is then approximated as Dirac's delta function[15], that is, $\dot{G}_{jl}^{\mathrm{calc}} \,\hat{\times}\, \dot{G}_{jl}^{\mathrm{true}} \approx \delta(t)$, then the HBP value should directly relate to the slip-rate $\dot{D}$ at the potential lth grid cell. This approximation is more appropriate than the one in the BP method[15]. We performed the synthetic test assuming the simple point source model for confirming our method, and the results are presented in Supplementary Figure S5 online.

The fault model. Unlike the conventional BP method, the HBP method uses Green's function to project the sources of high-frequency radiation. In general, Green's function depends on a depth and focal mechanism of an earthquake, so the fault geometry must be accurately determined. To construct the non-planar fault model, we used a model of subducting plate geometry called SLAB[20], which is constrained by seismic data and forward gravity modeling. To interpolate the sparsely distributed SLAB geometry (longitude, latitude, and depth) onto a regular grid with node spacing of 0.02°, we used the adjustable tension continuous curvature surface gridding algorithm of the Generic Mapping Tools[36]. The rake angle in each grid cell was determined by both the geometry of the fault surface and the direction of plate motion, referring global plate motion model NNR-NUVEL-1A[37]. The important technical improvement of this study is that we set a grid spacing of 3 km, while the former HBP study[16] used a coarser 10 km spacing. If we consider the P-wave speed as 8 km/s and high-frequency waves at about 1 Hz, at least half-wave length of grid spacing, i.e., 4 km spacing would be needed for imaging the high-frequency radiation. So the finer-grid spacing set in this study can ensure the necessary resolution, and the behavior of high-frequency radiation can be well extracted by our method. In other words, 10 km spacing is not fine enough to image the heterogeneous distribution of high-frequency radiation in both the HBP and the BP methods.

1. Madariaga, R. High-frequency radiation from crack (stress drop) models of earthquake faulting. *Geophys. J. Int.* **51**, 625–651 (1977).

2. Yamashita, T. High-frequency acceleration radiated by unsteadily propagating cracks and its near-source geometricale attenuation. *J. Phys. Earth* **31**, 1–32 (1983).

3. Bernard, P. & Madariaga, R. A new asymptotic method for the modeling of near-field accelerograms. *Bull. Seismol. Soc. Am.* **74**, 539–557 (1984).

4. Spudich, P. & Frazer, L. Use of ray theory to calculate high-frequency radiation from earthquake sources having spatially variable rupture velocity and stress drop. *Bull. Seismol. Soc. Am.* **74**, 2061–2082 (1984).

5. Olson, A. & Apsel, R. Finite faults and inverse theory with applications to the 1979 Imperial Valley earthquake. *Bull. Seismol. Soc. Am.* **72**, 1969–2001 (1982).

6. Hartzell, S. & Heaton, T. Inversion of strong ground motion and teleseismic waveform data for the fault rupture history of the 1979 Imperial Valley, California, earthquake. *Bull. Seismol. Soc. Am.* **73**, 1553–1583 (1983).

7. Yagi, Y. & Fukahata, Y. Introduction of uncertainty of Green's function into waveform inversion for seismic source processes. *Geophys. J. Int.* **186**, 711–720 (2011).

8. Cirella, A., Piatanesi, A. & Tinti, E. Complexity of the rupture process during the 2009 L'Aquila, Italy, earthquake. *Geophys. J. Int.* **190**, 607–621 (2012).

9. Ishii, M., Shearer, P. M., Houston, H. & Vidale, J. E. Extent, duration and speed of the 2004 Sumatra-Andaman earthquake imaged by the Hi-Net array. *Nature* **435**, 933–936 (2005).

10. Yao, H., Shearer, P. M. & Gerstoft, P. Subevent location and rupture imaging using iterative backprojection for the 2011 Tohoku Mw 9.0 earthquake. *Geophys. J. Int.* **190**, 1152–1168 (2012).

11. Koper, K. D., Hutko, A. R., Lay, T. & Sufri, O. Imaging short-period seismic radiation from the 27 February 2010 Chile (Mw 8.8) earthquake by back-projection of P, PP, and PKIKP waves. *J. Geophys. Res.* **117**, B02308 (2012).

12. Xu, Y., Koper, K., Sufri, O., Zhu, L. & Hutko, A. Rupture imaging of the Mw 7.9 12 May 2008 Wenchuan earthquake from back projection of teleseismic P waves. *Geochem. Geophys. Geosyst.* **10**, Q04006 (2009).

13. Kiser, E. & Ishii, M. The 2010 Mw 8.8 Chile earthquake: Triggering on multiple segments and frequency-dependent rupture behavior. *Geophys. Res. Lett.* **38**, L07301 (2011).

14. Meng, L., Inbal, A. & Ampuero, J. A window into the complexity of the dynamic rupture of the 2011 Mw 9 Tohoku-Oki earthquake. *Geophys. Res. Lett.* **38**, L00G07 (2011).

15. Fukahata, Y., Yagi, Y. & Rivera, L. Theoretical relationship between back-projection imaging and classical linear inverse solutions. *Geophys. J. Int.* **196**, 552–559 (2014).

16. Yagi, Y., Nakao, A. & Kasahara, A. Smooth and rapid slip near the Japan Trench during the 2011 Tohoku-oki earthquake revealed by a hybrid back-projection method. *Earth Planet. Sci. Lett.* **355-356**, 94–101 (2012).

17. Suzuki, M. & Yagi, Y. Depth dependence of rupture velocity in deep earthquakes. *Geophys. Res. Lett.* **38**, L05308 (2011).

18. Lay, T. *et al*. Depth-varying rupture properties of subduction zone megathrust faults. *J. Geophys. Res.* **117**, B04311 (2012).

19. Uchide, T., Yao, H. & Shearer, P. Spatio-temporal distribution of fault slip and high-frequency radiation of the 2010 El Mayor-Cucapah, Mexico earthquake. *J. Geophys. Res.* **118**, 1–10 (2013).

20. Tassara, A. & Echaurren, A. Anatomy of the Andean subduction zone: three-dimensional density model upgraded and compared against global-scale models. *Geophys. J. Int.* **189**, 161–168 (2012).

21. Pulido, N., Yagi, Y., Kumagai, H. & Nishimura, N. Rupture process and coseismic deformations of the 27 February 2010 Maule earthquake, Chile. *Earth, Planets Sp.* **63**, 955–959 (2011).

22. Kikuchi, M. & Kanamori, H. Inversion of complex body waves—III. *Bull. Seismol. Soc. Am.* **81**, 2335–2350 (1991).

23. Kennett, B. Constraints on seismic velocities in the Earth from traveltimes. *Geophys. J. Int.* **122**, 108–124 (1995).

24. Bohm, M., Lüth, S., Echtler, H., Asch, G. & Bataille, K. The Southern Andes between 36 and 40 S latitude: seismicity and average seismic velocities. *Tectonophysics* **356**, 275–289 (2002).

25. Kiser, E. & Ishii, M. The 2010 Maule, Chile, Coseismic Gap and Its Relationship to the 25 March 2012 Mw 7.1 Earthquake. *Bull. Seismol. Soc. Am.* **103**, 1148–1153 (2013).

26. Wang, D. & Mori, J. Frequency-dependent energy radiation and fault coupling for the 2010 Mw8.8 Maule, Chile, and 2011 Mw9.0 Tohoku, Japan, earthquakes. *Geophys. Res. Lett.* **38**, L22308 (2011).

27. Meng, L., Ampuero, J., Luo, Y., Wu, W. & Ni, S. Mitigating artifacts in back-projection source imaging with implications on frequency-dependent properties of the Tohoku-Oki earthquake. *Earth Planets Sp.* **64**, 1101–1109 (2012).

28. Ohnaka, M. & Yamashita, T. A cohesive zone model for dynamic shear faulting based on experimentally inferred constitutive relation and strong motion source parameters. *J. Geophys. Res.* **94**, 4089 (1989).

29. Gabriel, A.-A., Ampuero, J.-P., Dalguer, L. A. & Mai, P. M. Source properties of dynamic rupture pulses with off-fault plasticity. *J. Geophys. Res.* **118**, 4117–4126 (2013).

30. Husseini, M. The fracture energy of earthquakes. *Geophys. J. Int.* **43**, 367–385 (1975).

31. Fukuyama, E. & Madariaga, R. Rupture dynamics of a planar fault in a 3D elastic medium: rate-and slip-weakening friction. *Bull. Seismol. Soc. Am.* **88**, 1–17 (1998).

32. Ide, S. & Aochi, H. Earthquakes as multiscale dynamic ruptures with heterogeneous fracture surface energy. *J. Geophys. Res.* **110**, B11303 (2005).

33. Madariaga, R., Ampuero, J. & Adda-Bedia, M. Seismic radiation from simple models of earthquakes. *Geophys. Monogr. Ser.* **170**, 223–236 (2006).

34. Dunham, E. M., Belanger, D., Cong, L. & Kozdon, J. E. Earthquake Ruptures with Strongly Rate-Weakening Friction and Off-Fault Plasticity, Part 2: Nonplanar Faults. *Bull. Seismol. Soc. Am.* **101**, 2308–2322 (2011).

35. Muirhead, K. T. & Datt, R. The N-th root process applied to seismic array data. *Geophys. J. Int.* **47**, 197–210 (1976).

36. Wessel, P. & Smith, W. H. F. New, improved version of generic mapping tools released. *Eos, Trans. Am. Geophys. Union* **79**, 579–579 (1998).

37. DeMets, C., Gordon, R. G., Argus, D. F. & Stein, S. Effect of recent revisions to the geomagnetic reversal time scale on estimates of current plate motions. *Geophys. Res. Lett.* **21**, 2191–2194 (1994).

Acknowledgments

Author contributions

R.O. mainly performed the analysis and wrote the manuscript. Y.Y. provided the initial idea for this study and contributed to the interpretation. S.H. principally contributed to the interpretation of the result.

Additional information